

JGR Space Physics

RESEARCH ARTICLE

10.1029/2021JA029180

Key Points:

- Fully kinetic self-consistent simulations of the Reiner Gamma plasma environment
- The plasma environment is vastly different at different altitudes and depends critically on the upstream plasma
- Our work helps to define measurement requirements for future missions to magnetized regions of the lunar surface

Correspondence to:

J. Deca,
jandeca@gmail.com





Citation:

Deca, J., Poppe, A. R., Divin, A., & Lembège, B. (2021). The plasma environment surrounding the Reiner Gamma magnetic anomaly. *Journal of Geophysical Research: Space Physics*, 126, e2021JA029180. <https://doi.org/10.1029/2021JA029180>

Received 27 JAN 2021

Accepted 2 AUG 2021

The Plasma Environment Surrounding the Reiner Gamma Magnetic Anomaly

J. Deca^{1,2,3} , A. R. Poppe⁴ , A. Divin⁵ , and B. Lembège³ 

¹Laboratory for Atmospheric and Space Physics (LASP), University of Colorado Boulder, Boulder, CO, USA, ²Institute for Modeling Plasma, Atmospheres and Cosmic Dust, NASA/SSERVI, Silicon Valley, CA, USA, ³Laboratoire Atmosphères, Milieux, Observations Spatiales (LATMOS), Université de Versailles à Saint Quentin, Guyancourt, France, ⁴Space Sciences Laboratory, University of California at Berkeley, Berkeley, CA, USA, ⁵St. Petersburg State University, St. Petersburg, Russia

Abstract Reiner Gamma is a prime target for low-orbiting spacecraft or even surface-landed missions in the near future. The region hosts a prominent lunar swirl that is co-located with a strong and well-structured magnetic anomaly. We simulate and discuss Reiner Gamma's near-surface plasma environment at different altitudes above the lunar surface using the fully kinetic particle-in-cell code iPIC3D. The input magnetic field model is based on orbital-altitude observations from the Kaguya and Lunar Prospector missions. We develop eight simulation cases, representing the distinct plasma regimes. Reiner Gamma is exposed to along a typical orbit, including different solar wind incidence angles and the magnetosheath crossing. We show that the plasma environment is vastly different at different altitudes and depends critically on the upstream plasma parameters, consistent with the predictions of the solar wind standoff model. Our work helps to define measurement requirements for a possible future low-orbiting or lander mission to the Reiner Gamma area or similarly magnetized regions of the lunar surface.

Plain Language Summary The Reiner Gamma region on the lunar surface hosts a set of brightness variations, or “swirls,” that are co-located with a prominent crustal magnetic field. Recently, it has been identified as one of the prime locations to be visited by one of NASA's next lunar missions. Here, we analyze the distinct plasma regimes that such a mission may encounter along its trajectory, such as the Moon's crossing through the Earth's magnetosheath and a set of different solar wind directions. We simulate the electron, proton, and He²⁺ dynamics with computational particles and include the Reiner Gamma magnetic field using a model developed from Kaguya and Lunar Prospector measurements. We find that the plasma environment is vastly different at different altitudes and depends critically on the upstream plasma parameters. Our models are essential to help define the measurement requirements for future endeavors to magnetized regions on the lunar surface, such as Reiner Gamma.

1. Introduction

The Apollo missions first measured the magnitude of the lunar crustal magnetic fields (Dyal et al., 1970, 1974; Fuller, 1974; Sharp et al., 1973) after it was shown by the Luna 2 mission that no lunar global magnetic field currently exists (Dolginov & Pushkov, 1960). It is theorized, however, that these crustal magnetic anomalies (LMAs) may have formed in the presence of a now extinct dynamo field (Arkani-Hamed & Boutin, 2014; Baek et al., 2019; Hood, 2011; Hood et al., 2001; Kelley & Garrick-Bethell, 2020; Nayak et al., 2017), but little is known still about the geological origins of LMAs. The surface material may have become magnetized through thermoremanent magnetization of impact ejecta (Hood et al., 2001; Wicczorek et al., 2012) or volcanic materials (Hemingway & Tikoo, 2018; Purucker et al., 2012), or through shock-remanent magnetization by large impacts (Hood & Artemieva, 2008).

LMAs range up to a few hundreds of kilometers in size, which is relatively tiny compared to the lunar radius, and have estimated surface magnetic field strengths shy of one thousand nanoTesla (Hood et al., 2001; Mitchell et al., 2008; Purucker & Nicholas, 2010; Tsunakawa et al., 2015). This makes the local plasma environment in which LMAs are embedded intriguing plasma-physics laboratories. The spatial scales of LMAs are smaller than the local ion inertial lengths and gyroradii, but the electron population is largely magnetized still. This results in an interaction regime with the impinging solar wind or magnetosphere plasma that

may be highly non-adiabatic (Chu et al., 2021; Deca & Divin, 2016; Deca et al., 2016; Howes et al., 2015; Kallio et al., 2012; Lue et al., 2016; Poppe et al., 2012; Saito et al., 2012). Driven by electron dynamics and the presence of an associated ambipolar electric field above primarily horizontal magnetic field geometries, a mini-magnetosphere may form and a significant fraction of the ion population population may be deflected away from the surface (Bamford et al., 2012; Deca et al., 2014, 2015; Hemingway & Garrick-Bethell, 2012; Kurata et al., 2005; Lin et al., 1998; Poppe et al., 2016; Usui et al., 2017; Zimmerman et al., 2015).

Lunar swirls are visually distinctive high-albedo surface markings that are always co-located with LMAs (Blewett et al., 2011; El-Baz, 1972; Hood & Schubert, 1980; Hood & Williams, 1989; Kramer, Besse, et al., 2011; Schultz & Srnka, 1980). Although no swirls have been found away from magnetized regions, not all LMAs host such albedo patterns (Blewett et al., 2011; Denevi et al., 2016). Their evolutionary scenarios have been shrouded in mystery, but are most surely connected with the crustal fields themselves (Pieters & Noble, 2016). The local electromagnetic and plasma environment may produce unique spectral properties (Pieters, Moriarty, & Garrick-Bethell, 2014) and magnetically (Pieters, Garrick-Bethell, & Hemingway, 2014) or electrostatically sort lofted high-albedo dust on the lunar surface (Garrick-Bethell et al., 2011; Hendrix et al., 2016). Recent cometary and micrometeoroid impacts may have left behind bright unweathered fine-grained material (Pinet et al., 2000; Schultz & Srnka, 1980; Starukhina & Shkuratov, 2004; Syal & Schultz, 2015), and the formation of mini-magnetospheres may cause the solar wind to standoff and locally change plasma weathering patterns and surface chemistry (Blewett et al., 2010, 2011; Deca et al., 2018, 2020; Hood & Schubert, 1980; Kramer, Besse, et al., 2011; Kramer, Combe, et al., 2011; Glotch et al., 2015; Hemingway & Garrick-Bethell, 2012; Hemingway et al., 2015; Hendrix et al., 2016; Pieters & Noble, 2016). The ability of the magnetic geometry to form a mini-magnetosphere provides a straightforward explanation why only some LMAs are found to be co-located with lunar swirls. If a sufficiently strong ambipolar electric field is not formed, the local solar wind weathering pattern remains unaltered (Deca et al., 2018). Evidence suggests that all these mechanisms may have their part in the joint evolution of LMAs and lunar swirls. For example, an increased amount of charged particle flux to the surface may be needed to accommodate and control the rate of surface weathering by impacts (Blewett et al., 2011; Glotch et al., 2015).

Reiner Gamma is a prominent lunar swirl formation with an overall length of about 70 km, located on the Oceanus Procellarum (7.5°N 59.0°W; see Figure 1 of Lee et al., 2019). Its main body consists of an inner bright lobe surrounded by two narrow dark lanes and two outer bright lobes (see Figures 1a–1b of Poppe et al., 2016 or Figure 2 of Deca et al., 2018). The magnetic geometry of the co-located swirls has a maximum intensity of ~500 nT (Tsunakawa et al., 2015) and its horizontal dipolar-like structure (Kurata et al., 2005) is critical in generating the ambipolar electric field that regulates differential plasma weathering of the regolith surface (Deca et al., 2018; Poppe et al., 2016). In addition, fully kinetic modeling of the solar wind interaction with the observation-based magnetic geometry has shown that these weathering patterns change significantly over the course of a lunar day (Deca et al., 2020). An integrated proton and helium ion flux profile to the surface is crucial to reproduce the brightness ratios between the inner and outer bright lobes, the dark lanes, and the mare background.

Simulations have established a logical connection between the observed albedo pattern and the plasma-physical processes that govern the plasma interaction with Reiner Gamma's near-surface magnetic fields. It suggests that the observed swirl patterns could be used to fine-tune surface magnetization models and, hence, the geologic origins of lunar magnetic anomalies (Hemingway & Tikoo, 2018). Unfortunately, thus far no comprehensive low altitude (below 20 km) or surface measurements of the magnetic field and plasma environment have been made post-Apollo to complement and complete our understanding of the solar wind interaction with LMAs and swirl formation. As Reiner Gamma is likely to be a prime target for future low-orbiting spacecraft and lunar landers (e.g., Blewett et al., 2019; Garrick-Bethell et al., 2019; Stubbs et al., 2018), in this work, we investigate further Reiner Gamma's near-surface plasma environment in order to help define measurement requirements for a possible future mission.

2. Methods

In order to capture both the ion and electron dynamics of the plasma interactions near the Reiner Gamma formation self-consistently, we use the 3-D fully kinetic, electromagnetic, semi-implicit particle-in-cell code iPIC3D (Markidis et al., 2010). The key features of the code for solar wind-body interactions include

Table 1
Overview of the Plasma Parameters Used in the Different Simulation Cases

Case	n (cm^{-3}) [e^- , p^+ , He^{2+}]	T (eV) [e^- , p^+ , He^{2+}]	$ v_{flow} $ (km s^{-1})	α ($^\circ$)	$ B_{IMF} $ (nT)
Z (SW)	(3.15, 3, 0.15)	(13, 3.5, 3.5)	350	45	3
A (SW)	(3.15, 3, 0.15)	(13, 3.5, 3.5)	350	75	0
B (SW)	(3.15, 3, 0.15)	(13, 3.5, 3.5)	350	60	0
C (SW)	(3.15, 3, 0.15)	(13, 3.5, 3.5)	350	45	0
D (SW)	(3.15, 3, 0.15)	(13, 3.5, 3.5)	350	30	0
E (SW)	(3.15, 3, 0.15)	(13, 3.5, 3.5)	350	15	0
F (SW)	(3.15, 3, 0.15)	(13, 3.5, 3.5)	350	0	0
G (MS)	(10.5, 10, 0.5)	(50, 100, 100)	150	55	0

Note. α is the incidence angle of the flow with respect to the surface normal. SW and MS indicate the solar wind and magnetosheath, respectively.

open boundary conditions that allow us to create a drifting Maxwellian plasma in a computational domain centered on the object (Deca et al., 2015; Divin et al., 2007) and the ability to decrease the numerical resolution beyond the Debye scales when investigating non-Debye-scale plasma processes (e.g., Deca et al., 2017, 2020; Lapenta et al., 2006). The Reiner Gamma magnetic topology is reproduced using a Surface Vector Mapping (SVM) model based on Kaguya and Lunar Prospector magnetic field measurements (Deca et al., 2018, 2020; Tsunakawa et al., 2014; 2015). We approximate the lunar surface with an absorbing sphere of radius $R = 1737.1$ km.

All simulations reported on in this work use an identical numerical setup and input magnetic field model for the Reiner Gamma magnetic topology. Only the upstream solar wind plasma conditions are varied between the different cases (Table 1). The simulation domain measures $200 \times 650 \times 650 \text{ km}^3$ with a resolution of $1.35 \times 1.35 \times 1.35 \text{ km}^3$. The simulation time step is $1.75 \times 10^{-5} \text{ s}$. Three plasma species are included: electrons, protons, and alpha (He^{2+}) particles. Their respective densities are represented in the simulation using 64 computational particles per cell per species. The proton (alpha)-to-electron mass ratio is reduced to 256 (1024) to meet our numerical restrictions. Note that cases A–G are identical to those defined in Deca et al. (2020) and that case Z adds an interplanetary magnetic field (IMF) to case C.

3. Results and Discussion

Simulation cases A to F cover one fourth of the lunar orbit in six 15° segments, which is the part of the Moon's trajectory when Reiner Gamma is exposed to pristine solar wind plasma (Figure 1 in Deca et al., 2020). We did not include an IMF, allowing us to single out the effects of the SVM model on the near-surface plasma environment. Only for case Z an IMF has been included for comparison purposes with case C. In the following subsections, we discuss the effects of the solar wind incidence angle on Reiner Gamma's plasma environment with altitude above the lunar surface (Sections 3.1 and 3.2). In the final Section 3.3, case G presents a scenario when the region is significantly affected by the hot and dense magnetosheath plasma.

3.1. Reiner Gamma at 45° Solar Wind Incidence Angle

Figure 1 presents an overview of the simulated region surrounding the Reiner Gamma magnetic anomaly (case Z in Table 1). The solar wind speed is $|v_{flow}| = 350 \text{ km s}^{-1}$ and has a 45° incidence angle to the surface in the ecliptic (XY) plane. Mapped as well is the simulated proton number density at the lunar surface. The IMF is chosen parallel to the surface at $|B_{IMF}| = 3 \text{ nT}$ and creates a magnetic null point above the LMA (Olshevsky et al., 2016). The presented set of magnetic field lines highlights the roughly dipolar structure of Reiner Gamma's main magnetic anomaly (Kurata et al., 2005), indicating the spatial locations of the inner bright lobe and the dark lanes (Deca et al., 2018). The density halo surrounding the inner bright lobe, that is, the location where the ambipolar electric field is anchored, is located roughly 15 km above the lunar surface for the chosen upstream plasma conditions (not shown; e.g., Figure 3 in Deca et al., 2018). This elec-

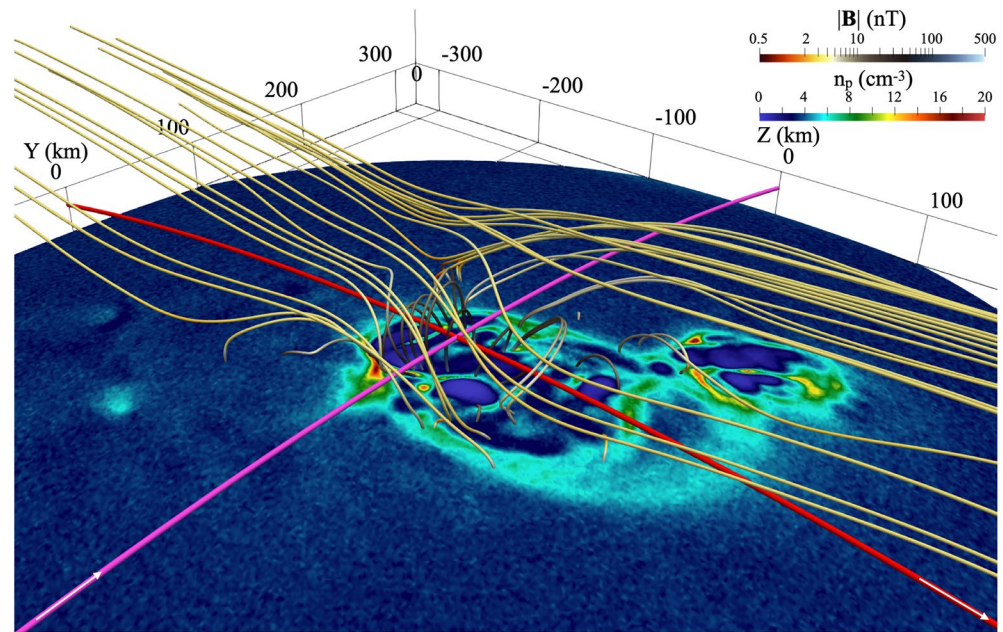


Figure 1. Overview of the simulated region surrounding the Reiner Gamma magnetic anomaly (case Z in Table 1). The solar wind incidence angle is 45° and the IMF is chosen parallel to the surface (a sample of field lines is shown for illustration, see Figure 5 and the accompanying discussion for quantitative insights). Two trajectories are indicated crossing the center of the main anomaly at 15 km above the spherical lunar surface. The polar and (near-)equatorial orbit are colored in magenta and red, respectively. n_p is the proton number density, shown here at the lunar surface. $|B|$ is the magnetic field magnitude. The origin of the coordinate system is set at (59° W, 7.5° N) on the surface. The X axis points away from the surface. The Y and Z directions are chosen along the polar and equatorial direction, respectively.

troshath has a thickness of 8 km or about one electron skin depth (Bamford et al., 2012; Deca et al., 2014). To investigate the plasma environment a low-orbiting spacecraft would encounter when flying through the Reiner Gamma region, we follow the evolution of a set of plasma parameters along a polar (magenta) and equatorial (red) orbit through the center of the main anomaly at 15 km above the surface. The results are shown in Figures 2 and 3, respectively.

Along the polar orbit (Y direction), the magnetic field profiles indicate a dipolar topology, with a maximum along Y and a polarity change along X, the direction perpendicular to the lunar surface (Figure 2b). At 15 km altitude we cross through the density halos formed above both the inner and outer bright lobes (Figure 2a). The magnitude of the ambipolar electric field along this trajectory measures 33 mV m^{-1} at maximum and is unable to significantly affect the He^{2+} density profile (Figures 2a and 2c). Particularly interesting is that the maxima of the electron and proton densities and the electric field do not exactly line up as due to the 45° solar wind incidence angle, charge separation between the ions and electrons is greatest at the upwind side of the anomaly (see also the discussion of Figure 3). Under normal solar wind incidence the maximum ambipolar electric field values are found lined up exactly with the density halo and the most horizontal magnetic field regions (Deca et al., 2018).

The energy distributions on the lower panels of Figure 2 are created by binning all computational particles by energy in a cylinder with radius 1 km around the orbit trajectory. The distribution is then split in a component streaming away (UP) and toward (DOWN) the lunar surface. Electrons move about with a thermal velocity much faster than the solar wind speed. The UP and DOWN energy distributions behave therefore very similar. Inside the density halo both parts of the electron distribution are equally heated by the interactions with the LMA (Figures 2d and 2e). The only significant differences are observed at $Y = -24 \text{ km}$ and $Y = 20 \text{ km}$, where the orbital trajectory intersects the density halo. These locations indicate the regions where the electrons are accelerated (rather than heated) by the $\mathbf{E} \times \mathbf{B}$ -drift mechanism (Deca et al., 2015). The ion thermal velocity is significantly smaller than the solar wind speed. Consequently, the UP and DOWN ion energy distributions show different features and complement the electron behavior (Figures 2f and 2g). We

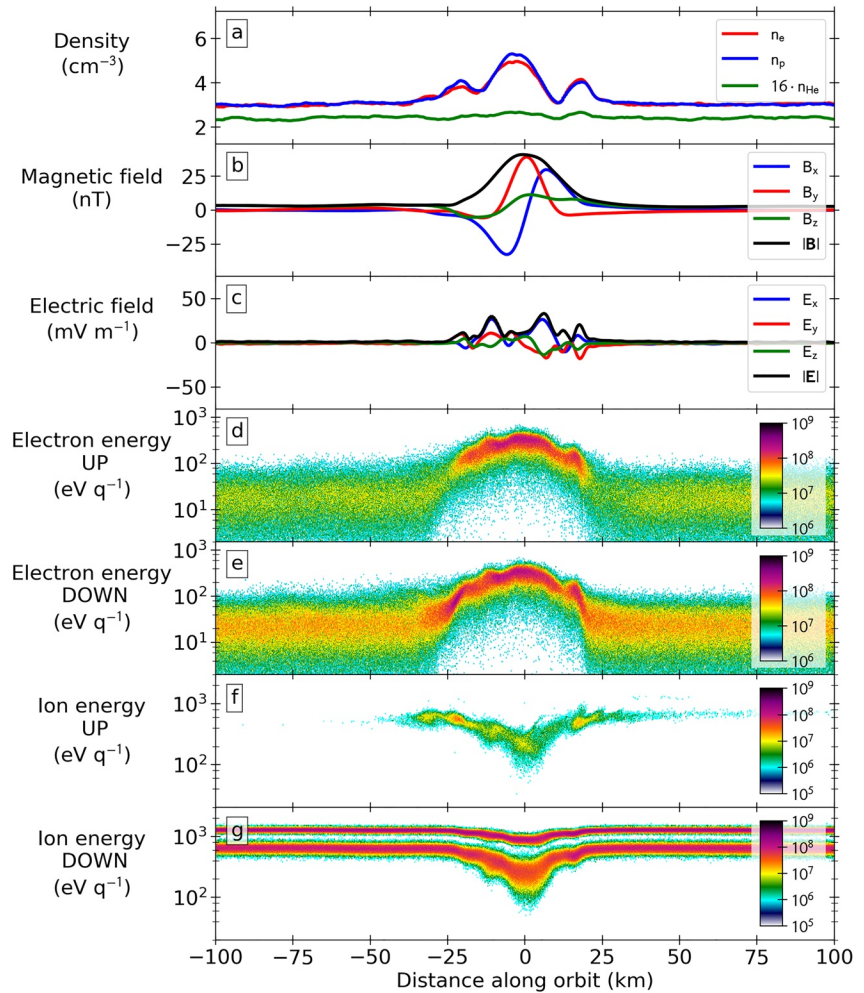


Figure 2. Line plots along the polar (Y direction; magenta) orbit indicated on Figure 1. The differential energy flux (color scale in the lower four panels) has units $eV cm^{-2} s^{-1} st^{-1} eV^{-1}$. All lines and distributions are snapshots recorded at the same time step after the simulations have reached steady state.

find that few to no He^{2+} ions and only 5%–10% of the protons have a velocity component directed away from the surface. Both ion populations are decelerated in the LMA interaction region, overshadowing the effects from non-adiabatic interactions that may locally cool or heat ions. Reflected protons streaming away from the LMA tend to regain their initial (pre-reflection) energy (Figure 2f). Note that the proton and He^{2+} gyroradii are significantly greater than the LMA interaction region. This indicates that electrostatic reflection is the responsible mechanism, without the magnetic field significantly altering the trajectories (Deca et al., 2015).

Along the equatorial orbit (Z direction) we observe larger density and electric field variations as compared to the polar orbit (Figures 3a and 3c). The solar wind impinges the magnetic topology under a 45° incidence angle in the ecliptic/equatorial (XZ) plane, creating an obstacle to overcome for the solar wind to reach the surface at this location. In response, the charge-separation ambipolar field is largest at the upwind boundary, measuring $69 mV m^{-1}$ at maximum. Consequently, also the density pile-up is larger on this side. Interestingly, we observe also a mini-wake at about $Z = 20 km$ followed by a focus point further downwind at $Z = 30 km$. Note that the He^{2+} mini-wake is shortest. Figure 4 presents a close-up view with a 2-D map of the He^{2+} number density perpendicular to the surface and along the equatorial orbit direction. It shows more clearly the locations where the density piles up as well as the mini-wake, where significantly fewer He^{2+} particles penetrate the magnetic structure. The behavior somewhat resembles the rotor often found on the lee-side of a mountain on Earth under windy conditions.

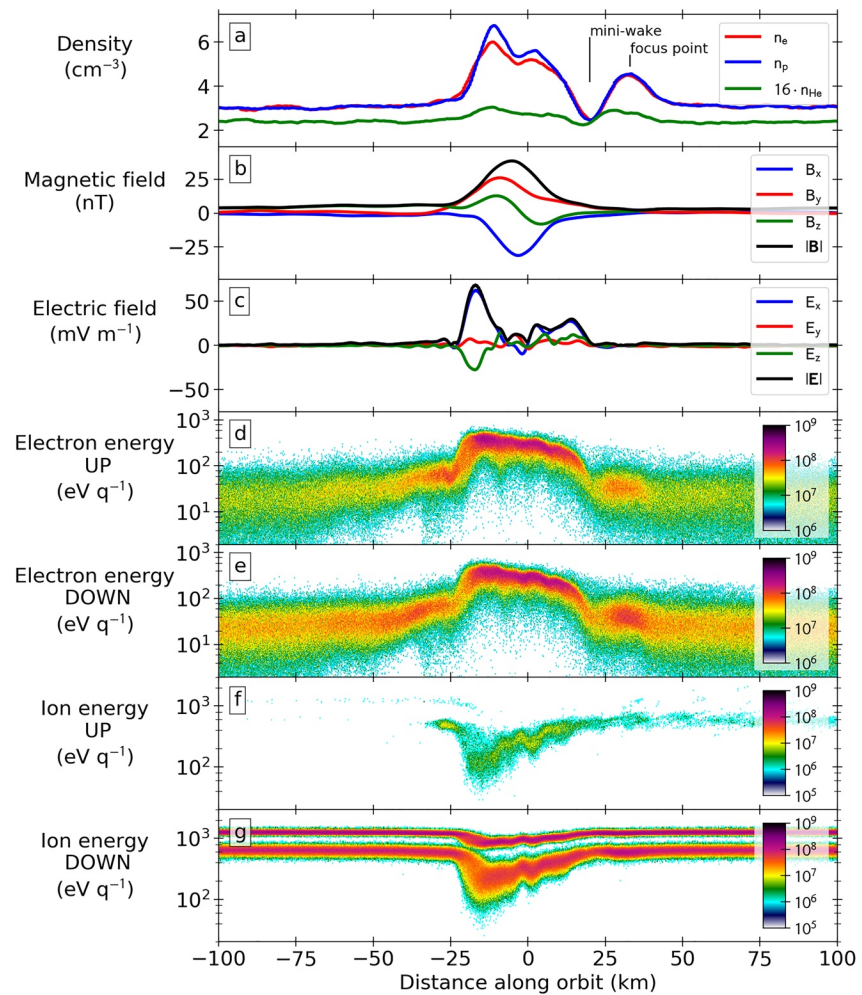


Figure 3. Line plots along the equatorial (Z direction; red) orbit are indicated in Figure 1. The differential energy flux (color scale in the lower four panels) has units $\text{eV cm}^{-2} \text{s}^{-1} \text{st}^{-1} \text{eV}^{-1}$. All lines and distributions are snapshots recorded at the same time step after the simulations have reached the steady state.

The electron energy distributions along the equatorial orbit (Figures 3d and 3e) show similar characteristics to the polar orbit, with most heating and a larger acceleration component found at the upwind side of the anomaly, where the $\mathbf{E} \times \mathbf{B}$ -drift starts pushing the electrons across the halo (Deca et al., 2014). The ion energy distributions (Figures 3f and 3g) are asymmetric as well, with most reflected particles found at the downwind side of Reiner Gamma ($Z > 0$). In addition, we observe a small amount of He^{2+} ions that seem secularly reflected at the upwind side of the anomaly, whereas few are present downwind.

Figure 5 presents maps of the magnetic and electric field magnitude at increasing altitudes above the surface, centered on the Reiner Gamma region. The first column of maps shows the initial (input) magnetic field, that is, the SVM model plus the IMF, followed by the magnetic field magnitude at steady-state (second column) and the difference between the two (third column). The fourth, rightmost column introduces the electric field magnitude. We find that even at 50 km altitude, the solar wind electric and magnetic fields are strongly perturbed by the presence of Reiner Gamma (Figures 5l and 5x). Given the chosen upstream plasma conditions, the main component of Reiner Gamma is easily detectable at this altitude. The weaker component, that is, the second dipolar-like structure (Kurata et al., 2005), becomes apparent only below 30 km above the surface. The difference $|\mathbf{B} - \mathbf{B}_0|$ reveals variations up to ± 10 nT, which are caused by the impinging solar wind plasma compressing and deforming the magnetic field topology. Roughly, in Figures 5m–5r the blue regions tend to correspond to areas where the magnetic structure is pushed closer to

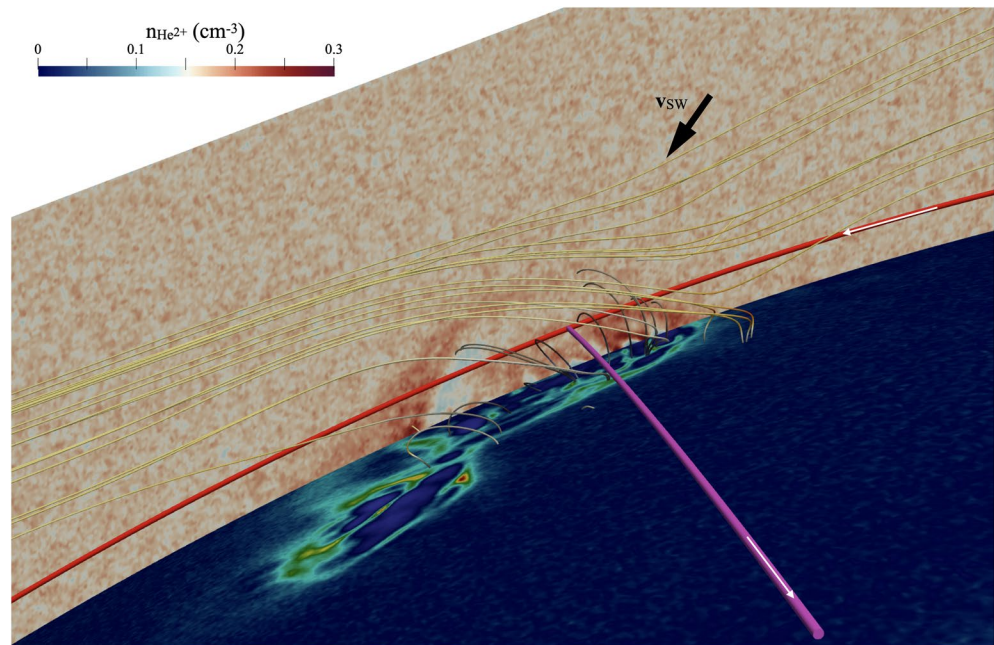


Figure 4. Close-up view including a 2-D map of the He^{2+} number density perpendicular to the surface and along the equatorial orbit direction. Identical to Figure 1, the surface presents the proton number density and both the polar and equatorial orbits are shown. The black arrow denotes the solar wind direction.

the surface, whereas the red regions indicate a more lateral deformation. The relative difference at 5 km above the surface indicates a 2%–3% change in the magnetic field magnitude compared to the input model (Figure 5m). The highest electric field magnitudes range up to 100 mV m^{-1} (Figures 5s–5x). The maxima are found on the upwind side of Reiner Gamma (top side of the panel in this representation), but at a different altitude for each component of the LMA. The main anomaly, that is, the tadpole's head, generates its density halo at the 10–20 km altitude, whereas the weaker component, that is, the tail region, produces most charge separation at 5 km above the surface.

3.2. Reiner Gamma at Different Solar Wind Incidence Angles

Figure 6 presents maps of the magnetic and electric field at increasing altitudes above the surface for different solar wind incidence angles. The letters in the yellow squares correspond to the case identifiers in Table 1, starting at a 75° solar wind incidence angle (case A) up to normal solar wind incidence (case F). The solar wind direction is chosen in the ecliptic plane. Note that we neglect the interplanetary and the magnetosphere magnetic field components to be able to evaluate most clearly the effects of the SVM model. These six simulations are representative of the periods Reiner Gamma is exposed to the solar wind plasma (see Figure 1 in Deca et al., 2020). The first column of each block reveals that the magnetic structure keeps its rough shape for all incidence angles. A mini-magnetosphere with fixed anchor points (the dark lanes) is formed in each case. Note, the chosen solar wind dynamic pressure of 0.74 nPa is on the lower edge of the measured range during quiet solar wind conditions. We anticipate that solar wind events will continuously alter the steady-state mini-magnetosphere structure. Deca et al. (2015) find that for a solar wind dynamic pressure of 2.4 nPa (their Run G) the height of the density halo above the surface reduces from 15 km to less than 5 km. The difference maps (middle columns) show that the more normal the solar wind incidence angle impinges on the lunar surface, the more compressed the magnetic structure becomes. A more shallow α results in mostly lateral deformations while greater deformations are found farther away from the surface. The differences with respect to the initial model stay below $\pm 10 \text{ nT}$ in absolute value, but become relatively larger with distance from the surface. The electric field maps (third column of each block) presents a similar story. A more shallow incidence angle leads to relatively weaker electric field magnitudes.

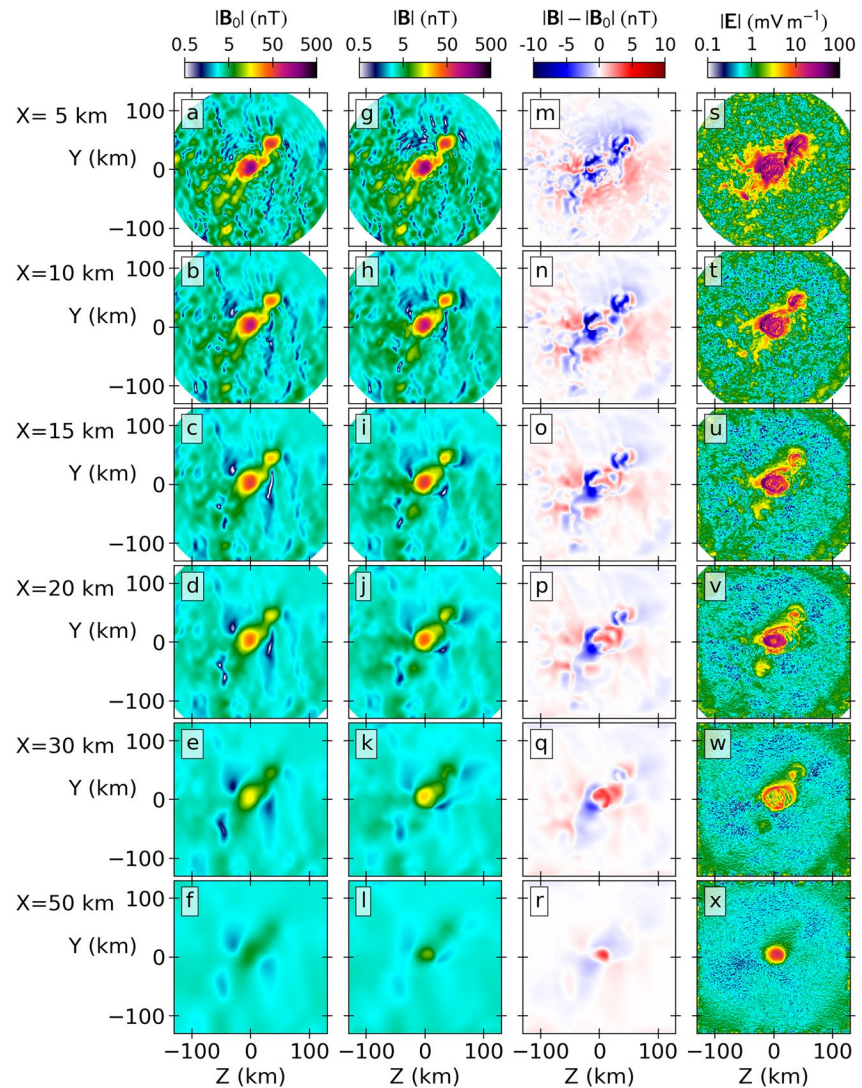


Figure 5. Maps of the magnetic and electric field at increasing altitudes above the surface (case Z in Table 1). (a–f) input Surface Vector Mapping magnetic field magnitude; (g–l) magnetic field magnitude at steady state; (m–r) difference between the magnetic field magnitude at steady state and the input magnetic field model (first column); (s–x) electric field magnitude.

3.3. Reiner Gamma in the Magnetosphere

Due to Reiner Gamma's westerly selenographic location, no significant amount of plasma flux impinges on the region throughout most of the Moon's magnetotail crossing (Table 1 and Figure 1 in Deca et al., 2020). We discuss here case G in Table 1, corresponding to the 2.5-day time frame during which Reiner Gamma is directly exposed to the hotter and denser magnetosheath plasma in between the magnetopause and the bow shock, on its way out of the terrestrial magnetosphere (Poppe et al., 2018). Note that compared to the solar wind cases, case G has a slower upstream plasma velocity, but similarly with no IMF included. Figures 7 and 8 present an overview of the plasma environment for this case, following the same format as Figures 3 and 5, respectively.

At 15 km above the lunar surface, we find that the magnetic field topology is much less compressed in the magnetosheath compared to the solar wind cases, because the upstream dynamic pressure measures only 0.45 nPa, compared to 0.74 nPa in the solar wind cases (Figure 7b). Although similar in structure, the magnetic field magnitude at this altitude is roughly twice as high as compared to cases A–F. A broad density halo is formed 30–40 km above the surface (not shown). This means that the density profiles of Figure 7a cut be-

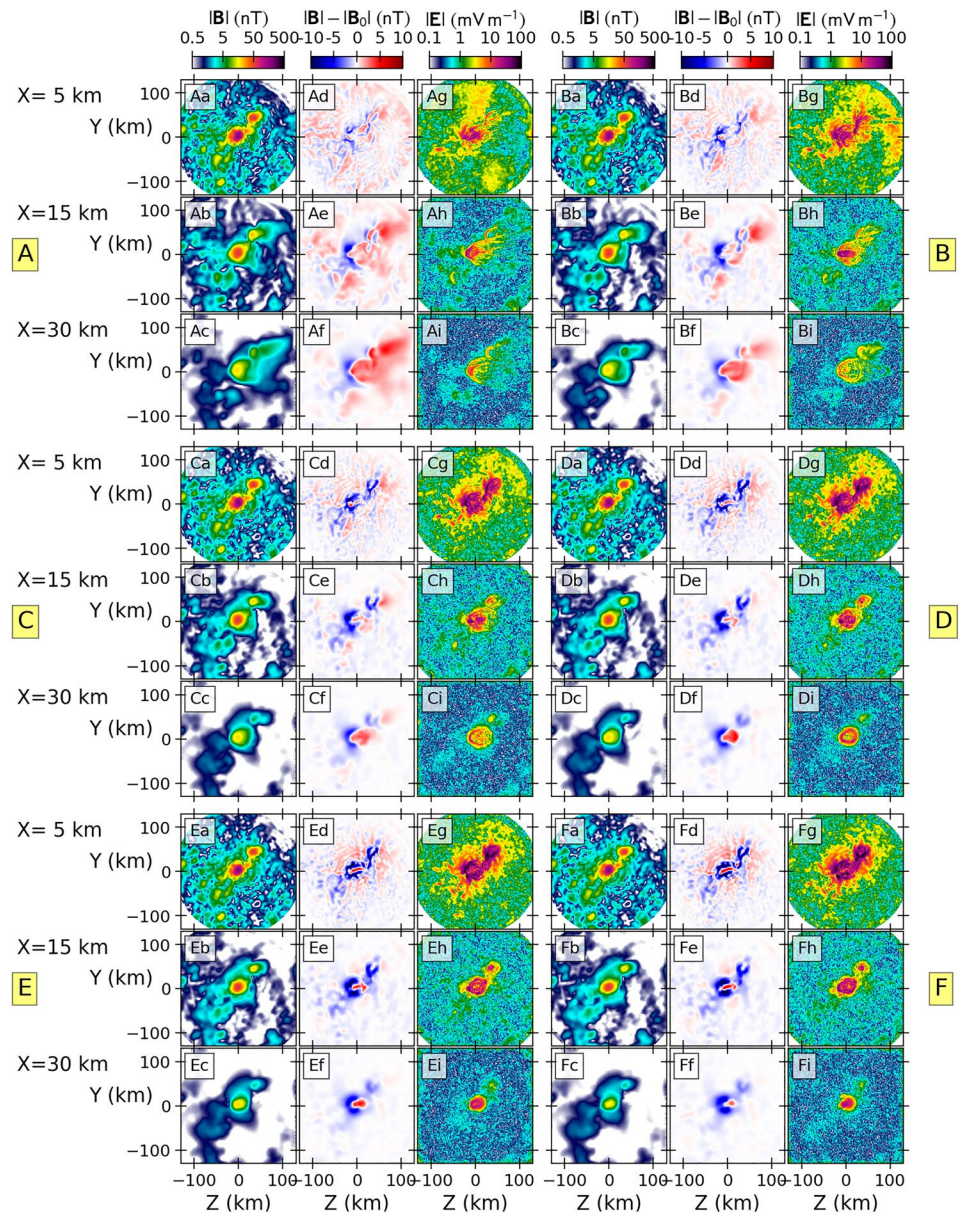


Figure 6. Maps of the magnetic and electric field at increasing altitudes above the surface for different solar wind incidence angles (cases a–f). The letters in the yellow squares correspond to the case identifiers in Table 1. The three columns in each block correspond to the magnetic field magnitude at steady state, the difference between the magnetic field magnitude at steady state and the Surface Vector Mapping magnetic field model and the electric field magnitude, respectively.

low the pile-up region and show a dip in density for all modeled species, rather than an increase. The wider structure is caused by the relatively low dynamic pressure. The maximum electric field magnitude at this altitude is 16 mV m^{-1} and coincides with the location of the highest magnetic field magnitude (Figures 7b and 7c). Compared to cases A–F, the electrons become heated/accelerated, indicating that a ∇B -mechanism might be responsible for the disturbances rather than a $\mathbf{E} \times \mathbf{B}$ drift (Deca et al., 2015). Only the very lowest energies are filtered away from the central anomaly region (Figures 7d and 7e). Due to the high thermal velocities, the proton and alpha populations are indistinguishable in the ion energy profiles (Figures 7f and 7g). In combination with the oblique incidence angle, both show a significant amount of particles with a velocity component away from the lunar surface. On the upwind side of the LMA the differential energy

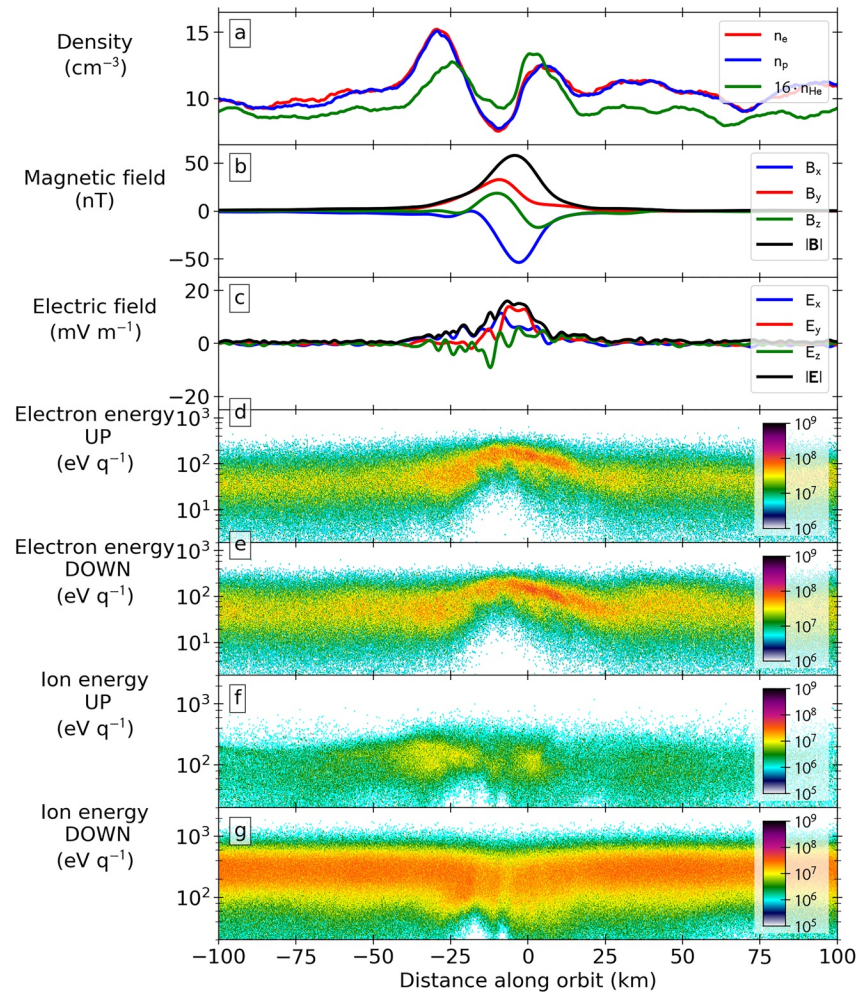


Figure 7. Line plots along the equatorial (red) orbit indicated on Figure 1 for case G. The differential energy flux (color scale in the lower four panels) has units $\text{eV cm}^{-2} \text{s}^{-1} \text{st}^{-1} \text{eV}^{-1}$. All lines and distributions are snapshots recorded at the same time step after the simulations have reached the steady state.

flux is elevated. Similar to the electrons, the lowest energy ions are disallowed from entering the region. Note that as we cross below the density halo, we do not observe the decelerated population seen in Figures 3f and 3g, which indicates that the ambipolar electric field is less efficient in the magnetosheath case.

Figure 8 presents maps of the magnetic and electric field at increasing altitudes above the surface for case G. The leftmost column shows clearly the structure of the SVM model as no IMF is included in this simulation case. At steady-state, the plasma interaction with the magnetic structure has caused a variety of fluctuations/instabilities throughout the simulation domain (panels g-i; to be reported on in a separate work). At 50 km above the lunar surface we find them to be of similar magnitude to the LMA magnetic field magnitude (Figure 7i). Note from Figure 8s that the setup of case G pushes the numerical boundaries of our simulation tool and creates a nonphysical electric field structure near the lunar surface downwind of the anomaly. The magnetosheath scenario does not produce enough plasma flow across the modeled surface in this area to keep the outflow boundary numerically stable (see Deca et al., 2015 for an in-depth discussion of the implementation and limitations of our boundary conditions). The ambipolar electric fields generated by the LMA show a similar evolution with altitude above the surface as the solar wind cases. The maximum electric field magnitude is found at the 5 km altitude and measures 60 mV m^{-1} . At 50 km we observe $|\mathbf{E}| = 4 \text{ mV m}^{-1}$. Finally, $|\mathbf{B}| - |\mathbf{B}_0|$ reveals magnetic field disturbances resembling the central bright lobe of Reiner Gamma up to 30 km altitude, whereas it is no longer observable in the simulated solar wind cases already at 15–20 km above the surface. The reason is the higher position of the density halo in case G.

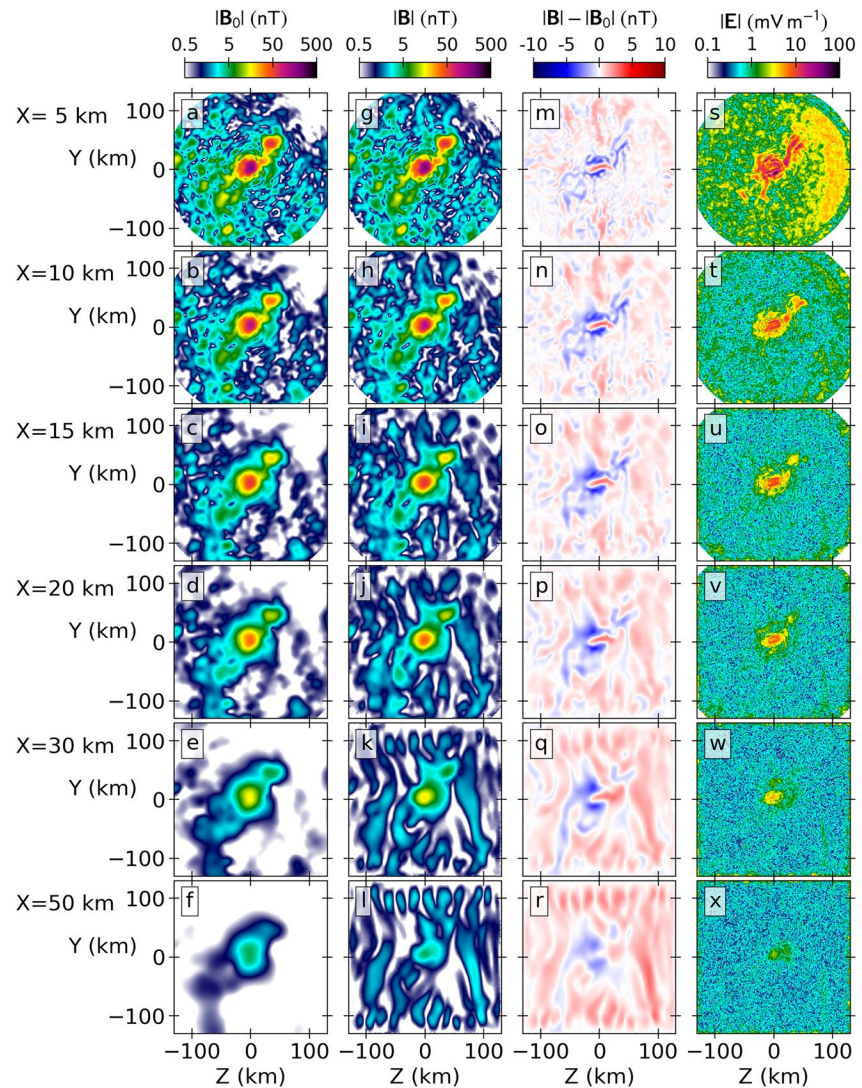


Figure 8. Maps of the magnetic and electric field at increasing altitudes above the surface for case G. (a–f) input Surface Vector Mapping magnetic field magnitude; (g–l) magnetic field magnitude at steady state; (m–r) difference between the magnetic field magnitude at steady state and the input magnetic field model (first column); (s–x) electric field magnitude.

As a result, when traversing the magnetosheath along a trajectory at lower (solar wind) dynamic pressures, surface magnetic field features can be detected up to twice farther from the surface in our simulation. In reality, however, the elevated magnetic field strength in the magnetosheath as compared to the solar wind IMF and the highly turbulent nature of the plasma downstream of the bow shock might make it more difficult to measure crustal magnetic fields at a given altitude.

4. Conclusions

In this work, we have discussed the plasma environment surrounding the Reiner Gamma magnetic anomaly using the fully kinetic particle-in-cell code iPIC3D, coupled with an SVM model of the near-surface magnetic field structure based on Kaguya and Lunar Prospector measurements. We covered the fraction of the lunar orbit when the region is exposed to a significant amount of plasma flux with eight different simulation cases that each represent a segment of the orbit, including different solar wind incidence angles and the hot and dense magnetosheath plasma.

Density and energy distribution profiles for the simulated electron, proton, and He²⁺ profiles, complimented with magnetic and electric field maps at increasing altitudes above the lunar surface, provide a detailed overview of the plasma environment. We show that (a) the situation is vastly different at different altitudes and (b) depends critically on the upstream plasma parameters. In addition, our findings are consistent with the predictions of the solar wind standoff model, that is, the plasma flux to the lunar surface is regulated by the ambipolar electric field generated by the solar wind plasma interaction with the magnetic field topology of Reiner Gamma (Deca et al., 2018).

Our work may help define measurement requirements for a possible future low-orbit or lander mission to the Reiner Gamma area or similarly magnetized regions of the lunar surface. Finally, note that although our fully kinetic approach allows us to resolve all relevant spatial and temporal scales of interest to study the solar wind plasma interaction with the Reiner Gamma magnetic anomaly, ultimately the predictive capabilities of the model are limited by the observations-based input magnetic field topology.

Data Availability Statement

All data necessary to validate the findings presented in this manuscript can be found at <https://doi.org/10.5281/zenodo.4474845> in accordance with the FAIR data project.

Acknowledgments

J. Deca gratefully acknowledges the support from NASA's Lunar Data Analysis Program, grant number 80NS-SC17K0420. A. Divin was supported by the RFBR Grant 19-02-00993. This work was supported in part by NASA's Solar System Exploration Research Virtual Institute (SSERVI): Institute for Modeling Plasmas, Atmosphere, and Cosmic Dust (IMPACT), grant number NNA14AB06A. Resources supporting this work were provided by the NASA High-End Computing (HEC) Program through the NASA Advanced Supercomputing (NAS) Division at Ames Research Center and by TGCC and CINES under the DARI project #A0050400295.

References

- Arkani-Hamed, J., & Boutin, D. (2014). Analysis of isolated magnetic anomalies and magnetic signatures of impact craters: Evidence for a core dynamo in the early history of the Moon. *Icarus*, 237, 262–277. <https://doi.org/10.1016/j.icarus.2014.04.046>
- Baek, S.-M., Kim, K.-H., Garrick-Bethell, I., & Jin, H. (2019). Magnetic anomalies within the crism basin: Magnetization directions, source depths, and ages. *Journal of Geophysical Research: Planets*, 124(2), 223–242. <https://doi.org/10.1029/2018JE005678>
- Bamford, R. A., Kellett, B., Bradford, W. J., Norberg, C., Thornton, A., Gibson, K. J., et al. (2012). Minimagnetospheres above the lunar surface and the formation of lunar swirls. *Physical Review Letters*, 109(8), 081101. <https://doi.org/10.1103/PhysRevLett.109.081101>
- Blewett, D. T., Coman, E. I., Hawke, B. R., Gillis-Davis, J. J., Purucker, M. E., & Hughes, C. G. (2011). Lunar swirls: Examining crustal magnetic anomalies and space weathering trends. *Journal of Geophysical Research*, 116. <https://doi.org/10.1029/2010JE003656>
- Blewett, D. T., Denevi, B. W., Robinson, M. S., Ernst, C. M., Purucker, M. E., & Solomon, S. C. (2010). The apparent lack of lunar-like swirls on Mercury: Implications for the formation of lunar swirls and for the agent of space weathering. *Icarus*, 209, 239–246. <https://doi.org/10.1016/j.icarus.2010.03.008>
- Blewett, D. T., Halekas, J., Greenhagen, B. T., Anderson, B. J., Denevi, B. W., Hurley, D. M., et al. (2019). Magnetic anomaly as natural laboratory: The lunar compass mission concept. In *Lunar and Planetary Science Conference* (Vol. 50, p. 1450).
- Chu, F., Halekas, J. S., Cao, X., McFadden, J. P., Bonnell, J. W., & Glassmeier, K. H. (2021). Electrostatic waves and electron heating observed over lunar crustal magnetic anomalies. *Journal of Geophysical Research: Space Physics*, 126(4), e28880. <https://doi.org/10.1029/2020JA028880>
- Deca, J., & Divin, A. (2016). Reflected charged particle populations around dipolar lunar magnetic anomalies. *The Astrophysical Journal*, 829, 60. <https://doi.org/10.3847/0004-637X/829/2/60>
- Deca, J., Divin, A., Henri, P., Eriksson, A., Markidis, S., Olshevsky, V., & Horányi, M. (2017). Electron and ion dynamics of the solar wind interaction with a weakly outgassing comet. *Physical Review Letters*, 118(20), 205101. <https://doi.org/10.1103/PhysRevLett.118.205101>
- Deca, J., Divin, A., Lapenta, G., Lembège, B., Markidis, S., & Horányi, M. (2014). Electromagnetic particle-in-cell simulations of the solar wind interaction with lunar magnetic anomalies. *Physical Review Letters*, 112(15), 151102. <https://doi.org/10.1103/PhysRevLett.112.151102>
- Deca, J., Divin, A., Lembège, B., Horányi, M., Markidis, S., & Lapenta, G. (2015). General mechanism and dynamics of the solar wind interaction with lunar magnetic anomalies from 3-d pic simulations. *Journal of Geophysical Research: Space Physics*, 120, 6443–6463. <https://doi.org/10.1002/2015JA021070>
- Deca, J., Divin, A., Lue, C., Ahmadi, T., & Horányi, M. (2018). Reiner Gamma albedo features reproduced by modeling solar wind standoff. *Nature Communications Physics*, 1(12). <https://doi.org/10.1038/s42005-018-0012-9>
- Deca, J., Divin, A., Wang, X., Lembège, B., Markidis, S., Horányi, M., & Lapenta, G. (2016). Three-dimensional full-kinetic simulation of the solar wind interaction with a vertical dipolar lunar magnetic anomaly. *Geophysical Research Letters*, 43, 4136–4144. <https://doi.org/10.1002/2016GL068535>
- Deca, J., Hemingway, D., Divin, A., Lue, C., Poppe, A., Garrick-Bethell, I., et al. (2020). Simulating the Reiner Gamma swirl: The long-term effect of solar wind standoff. *Journal of Geophysical Research: Planets*, 125(5), e2019JE006219. <https://doi.org/10.1029/2019JE006219>
- Denevi, B. W., Robinson, M. S., Boyd, A. K., Blewett, D. T., & Klima, R. L. (2016). The distribution and extent of lunar swirls. *Icarus*, 273, 53–67. <https://doi.org/10.1016/j.icarus.2016.01.017>
- Divin, A. V., Sitnov, M. I., Swisdak, M., & Drake, J. F. (2007). Reconnection onset in the magnetotail: Particle simulations with open boundary conditions. *Geophysical Research Letters*, 34, 9109. <https://doi.org/10.1029/2007GL029292>
- Dolginov, S. S., & Pushkov, N. V. (1960). Magnetic field of the outer corpuscular region. *International Cosmic Ray Conference*, 3, 30.
- Dyal, P., Parkin, C. W., & Daily, W. D. (1974). Magnetism and the interior of the moon. *Reviews of Geophysics and Space Physics*, 12, 568–591. <https://doi.org/10.1029/RG012i004p005688>
- Dyal, P., Parkin, C. W., & Sonett, C. P. (1970). Apollo 12 Magnetometer: Measurement of a steady magnetic field on the surface of the Moon. *Science*, 169, 762–764. <https://doi.org/10.1126/science.169.3947.762>

- El-Baz, F. (1972). The Alhazen to Abul Wafa swirl belt: An extensive field of light-colored sinuous markings. *NASA Special Publication*, 315, 2993.
- Fuller, M. (1974). Lunar magnetism. *Reviews of Geophysics*, 12(1), 23–70. <https://doi.org/10.1029/rg012i001p00023>
- Garrick-Bethell, I., Head, J. W., & Pieters, C. M. (2011). Spectral properties, magnetic fields, and dust transport at lunar swirls. *Icarus*, 212, 480–492. <https://doi.org/10.1016/j.icarus.2010.11.036>
- Garrick-Bethell, I., Paige, D. A., & Burton, M. E. (2019). NanoSWARM: A Proposed discovery mission to study space weathering, lunar water, lunar magnetism, and small-scale magnetospheres. In *Lunar and Planetary Science Conference* (Vol. 50, p. 2786).
- Glotch, T. D., Bandfield, J. L., Lucey, P. G., Hayne, P. O., Greenhagen, B. T., Arnold, J. A., et al. (2015). Formation of lunar swirls by magnetic field standoff of the solar wind. *Nature Communications*, 6, 6189. <https://doi.org/10.1038/ncomms7189>
- Hemingway, D. J., & Garrick-Bethell, I. (2012). Magnetic field direction and lunar swirl morphology: Insights from Airy and Reiner Gamma. *Journal of Geophysical Research*, 117(16), 10012. <https://doi.org/10.1029/2012JE004165>
- Hemingway, D. J., Garrick-Bethell, I., & Kreslavsky, M. A. (2015). Latitudinal variation in spectral properties of the lunar maria and implications for space weathering. *Icarus*, 261, 66–79. <https://doi.org/10.1016/j.icarus.2015.08.004>
- Hemingway, D. J., & Tikoo, S. M. (2018). Lunar swirl morphology constrains the geometry, magnetization, and origins of lunar magnetic anomalies. *Journal of Geophysical Research: Planets*, 123(8), 2223–2241. <https://doi.org/10.1029/2018JE005604>
- Hendrix, A., Greathouse, T., Retherford, K., Mandt, K., Gladstone, G., Kaufmann, D., et al. (2016). Lunar swirls: Far-uv characteristics. *Icarus*, 273, 68–74. <https://doi.org/10.1016/j.icarus.2016.01.003>
- Hood, L. L. (2011). Central magnetic anomalies of Nectarian-aged lunar impact basins: Probable evidence for an early core dynamo. *Icarus*, 211, 1109–1128. <https://doi.org/10.1016/j.icarus.2010.08.012>
- Hood, L. L., & Artemieva, N. A. (2008). Antipodal effects of lunar basin-forming impacts: Initial 3D simulations and comparisons with observations. *Icarus*, 193, 485–502. <https://doi.org/10.1016/j.icarus.2007.08.023>
- Hood, L. L., & Schubert, G. (1980). Lunar magnetic anomalies and surface optical properties. *Science*, 208, 49–51. <https://doi.org/10.1126/science.208.4439.49>
- Hood, L. L., & Williams, C. R. (1989). The lunar swirls—Distribution and possible origins. In G. Ryder, & V. L. Sharpton (Eds.), *Lunar and planetary science conference proceedings* (Vol. 19, pp. 99–113).
- Hood, L. L., Zakharian, A., Halekas, J., Mitchell, D. L., Lin, R. P., Acuña, M. H., & Binder, A. B. (2001). Initial mapping and interpretation of lunar crustal magnetic anomalies using Lunar Prospector magnetometer data. *Journal of Geophysical Research*, 106, 27825–27840. <https://doi.org/10.1029/2000JE001366>
- Howes, C. T., Wang, X., Deca, J., & Horányi, M. (2015). Laboratory investigation of lunar surface electric potentials in magnetic anomaly regions. *Geophysical Research Letters*, 42, 4280–4287. <https://doi.org/10.1002/2015GL063943>
- Kallio, E., Jarvinen, R., Dyadechkin, S., Wurz, P., Barabash, S., Alvarez, F., et al. (2012). Kinetic simulations of finite gyroradius effects in the lunar plasma environment on global, meso, and microscales. *Planetary and Space Science*, 74, 146–155. <https://doi.org/10.1016/j.pss.2012.09.012>
- Kelley, M. R., & Garrick-Bethell, I. (2020). Gravity constraints on the age and formation of the Moon's Reiner Gamma magnetic anomaly. *Icarus*, 338, 113465. <https://doi.org/10.1016/j.icarus.2019.11.3465>
- Kramer, G. Y., Besse, S., Dhringra, D., Nettles, J., Klima, R., Garrick-Bethell, I., et al. (2011). Spectral analysis of lunar swirls and the link between optical maturation and surface hydroxyl formation at magnetic anomalies. *Journal of Geophysical Research*, 116, E00G18. <https://doi.org/10.1029/2010JE003729>
- Kramer, G. Y., Combe, J.-P., Harnett, E. M., Hawke, B. R., Noble, S. K., Blewett, D. T., et al. (2011). Characterization of lunar swirls at Mare Ingenii: A model for space weathering at magnetic anomalies. *Journal of Geophysical Research*, 116, E04008. <https://doi.org/10.1029/2010JE003669>
- Kurata, M., Tsunakawa, H., Saito, Y., Shibuya, H., Matsushima, M., & Shimizu, H. (2005). Mini-magnetosphere over the Reiner Gamma magnetic anomaly region on the Moon. *Geophysical Research Letters*, 32, 24205. <https://doi.org/10.1029/2005GL024097>
- Lapenta, G., Brackbill, J. U., & Ricci, P. (2006). Kinetic approach to microscopic-macroscopic coupling in space and laboratory plasmas. *Physics of Plasmas*, 13(5), 055904. <https://doi.org/10.1063/1.2173623>
- Lee, J.-K., Maxwell, R., Jin, H., Baek, S.-M., Ghassemi, O., Kelley, M., et al. (2019). A small lunar swirl and its implications for the formation of the Reiner Gamma magnetic anomaly. *Icarus*, 319, 869–884. <https://doi.org/10.1016/j.icarus.2018.09.015>
- Lin, R. P., Mitchell, D. L., Curtis, D. W., Anderson, K. A., Carlson, C. W., McFadden, J., et al. (1998). Lunar surface magnetic fields and their interaction with the solar wind: Results from lunar prospector. *Science*, 281, 1480–1484. <https://doi.org/10.1126/science.281.5382.1480>
- Lue, C., Futaana, Y., Barabash, S., Saito, Y., Nishino, M., Wieser, M., et al. (2016). Scattering characteristics and imaging of energetic neutral atoms from the Moon in the terrestrial magnetosheath. *Journal of Geophysical Research: Space Physics*, 121(1), 432–445. <https://doi.org/10.1002/2015JA021826>
- Markidis, S., Lapenta, G., & Rizwan, U. (2010). Multi-scale simulations of plasma with iPIC3D. *Mathematics and Computers in Simulation*, 80(7), 1509–1519. <https://doi.org/10.1016/j.matcom.2009.08.038>
- Mitchell, D. L., Halekas, J. S., Lin, R. P., Frey, S., Hood, L. L., Acuña, M. H., & Binder, A. (2008). Global mapping of lunar crustal magnetic fields by Lunar Prospector. *Icarus*, 194, 401–409. <https://doi.org/10.1016/j.icarus.2007.10.027>
- Nayak, M., Hemingway, D., & Garrick-Bethell, I. (2017). Magnetization in the South Pole-Aitken basin: Implications for the lunar dynamo and true polar wander. *Icarus*, 286, 153–192. <https://doi.org/10.1016/j.icarus.2016.09.038>
- Olshevsky, V., Deca, J., Divin, A., Peng, I. B., Markidis, S., Innocenti, M. E., et al. (2016). Magnetic null points in kinetic simulations of space plasmas. *The Astrophysical Journal*, 819, 52. <https://doi.org/10.3847/0004-637X/819/1/52>
- Pieters, C. M., Garrick-Bethell, I., & Hemingway, D. (2014). Magnetic sorting of the regolith on the Moon: Lunar swirls. In *Agu fall meeting abstracts* (Vol. 2014, pp. P11D–10).
- Pieters, C. M., Moriarty, D. P., & Garrick-Bethell, I. (2014). Atypical regolith processes hold the key to enigmatic lunar swirls. In *Lunar and Planetary Science Conference* (p. 1408).
- Pieters, C. M., & Noble, S. K. (2016). Space weathering on airless bodies. *Journal of Geophysical Research: Planets*, 121, 1865–1884. <https://doi.org/10.1002/2016JE005128>
- Pinet, P. C., Shevchenko, V. V., Chevrel, S. D., Daydou, Y., & Rosemberg, C. (2000). Local and regional lunar regolith characteristics at Reiner Gamma formation: Optical and spectroscopic properties from Clementine and Earth-based data. *Journal of Geophysical Research*, 105, 9457–9476. <https://doi.org/10.1029/1999JE001086>
- Poppe, A. R., Farrell, W. M., & Halekas, J. S. (2018). Formation timescales of amorphous rims on lunar grains derived from Artemis observations. *Journal of Geophysical Research: Planets*, 123(1), 37–46. <https://doi.org/10.1002/2017JE005426>

- Poppe, A. R., Fatemi, S., Garrick-Bethell, I., Hemingway, D., & Holmström, M. (2016). Solar wind interaction with the Reiner gamma crustal magnetic anomaly: Connecting source magnetization to surface weathering. *Icarus*, *266*, 261–266. <https://doi.org/10.1016/j.icarus.2015.11.005>
- Poppe, A. R., Halekas, J. S., Delory, G. T., & Farrell, W. M. (2012). Particle-in-cell simulations of the solar wind interaction with lunar crustal magnetic anomalies: Magnetic cusp regions. *Journal of Geophysical Research*, *117*, 9105. <https://doi.org/10.1029/2012JA017844>
- Purucker, M. E., Head, I., James, W., & Wilson, L. (2012). Magnetic signature of the lunar South Pole-Aitken basin: Character, origin, and age. *Journal of Geophysical Research*, *117*(E5), E05001. <https://doi.org/10.1029/2011JE003922>
- Purucker, M. E., & Nicholas, J. B. (2010). Global spherical harmonic models of the internal magnetic field of the Moon based on sequential and coestimation approaches. *Journal of Geophysical Research*, *115*(14), 12007. <https://doi.org/10.1029/2010JE003650>
- Saito, Y., Nishino, M. N., Fujimoto, M., Yamamoto, T., Yokota, S., Tsunakawa, H., et al. (2012). Simultaneous observation of the electron acceleration and ion deceleration over lunar magnetic anomalies. *Earth Planets and Space*, *64*, 83–92. <https://doi.org/10.5047/eps.2011.07.011>
- Schultz, P. H., & Srnka, L. J. (1980). Cometary collisions on the moon and Mercury. *Nature*, *284*, 22–26. <https://doi.org/10.1038/284022a0>
- Sharp, L. R., Coleman, P. J., Jr., Lichtenstein, B. R., Russell, C. T., & Schubert, G. (1973). Orbital mapping of the lunar magnetic field. *The Moon*, *7*, 322–341. <https://doi.org/10.1007/BF00564638>
- Starukhina, L. V., & Shkuratov, Y. G. (2004). Swirls on the Moon and Mercury: Meteoroid swarm encounters as a formation mechanism. *Icarus*, *167*, 136–147. <https://doi.org/10.1016/j.icarus.2003.08.022>
- Stubbs, T. J., Malphrus, B. K., Hoyt, R., Mesarch, M. A., Tsay, M., Chai, D. J., et al. (2018). Bi-Sat Observations of the Lunar Atmosphere Above Swirls (BOLAS): Tethered SmallSat investigation of hydration and space weathering processes at the Moon. In *Lunar and Planetary Science Conference* (Vol. 49, p. 2394).
- Syal, M. B., & Schultz, P. H. (2015). Cometary impact effects at the moon: Implications for lunar swirl formation. *Icarus*, *257*, 194–206. <https://doi.org/10.1016/j.icarus.2015.05.005>
- Tsunakawa, H., Takahashi, F., Shimizu, H., Shibuya, H., & Matsushima, M. (2014). Regional mapping of the lunar magnetic anomalies at the surface: Method and its application to strong and weak magnetic anomaly regions. *Icarus*, *228*, 35–53. <https://doi.org/10.1016/j.icarus.2013.09.026>
- Tsunakawa, H., Takahashi, F., Shimizu, H., Shibuya, H., & Matsushima, M. (2015). Surface vector mapping of magnetic anomalies over the Moon using Kaguya and Lunar Prospector observations. *Journal of Geophysical Research: Planets*, *120*, 1160–1185. <https://doi.org/10.1002/2014JE004785>
- Usui, H., Miyake, Y., Nishino, M. N., Matsubara, T., & Wang, J. (2017). Electron dynamics in the minimagnetosphere above a lunar magnetic anomaly. *Journal of Geophysical Research: Space Physics*, *122*, 1555–1571. <https://doi.org/10.1002/2016JA022927>
- Wieczorek, M. A., Weiss, B. P., & Stewart, S. T. (2012). An impactor origin for lunar magnetic anomalies. *Science*, *335*(6073), 1212–1215. <https://doi.org/10.1126/science.1214773>
- Zimmerman, M. I., Farrell, W. M., & Poppe, A. R. (2015). Kinetic simulations of kilometer-scale minimagnetosphere formation on the moon. *Journal of Geophysical Research: Planets*, *120*(11), 1893–1903. <https://doi.org/10.1002/2015JE004865>